8

Holographic Three-Dimensional Measurement of an Optically Trapped Nanoparticle

Yoshio Hayasaki
Center for Optical Research and Education (CORE), Utsunomiya University, Japan

8.1 Introduction

The "Optical tweezers" technique [1] is a well-known technique used to trap and manipulate minute objects in a liquid without contact. It has been used for manipulating viruses and bacteria [2], single RNA molecules [3,4], and DNA molecules [5]. It has also been used to study the motion of the biological motor protein kinesin [6] and to sequence DNA [7]. It has been employed in not only biological applications but also for sorting objects in microfluidic systems [8–10], and measuring the mechanical properties [11] and shapes of microstructures [12]. Holographic optical tweezers [13–15] have also been used to create arbitrary three-dimensional structures [16–18].

In these applications, precise position measurement of the trapped object expands the ability to perform mechanical and structural measurements, and several methods have been developed. Position measurement with a quadrant photodiode (QPD) has been performed using spatial changes in light intensity according to the displacement of the trapped object with high temporal resolution and high sensitivity [1,19–23]. However, it is difficult to measure many objects simultaneously and to measure a three-dimensional (3D) position.

The use of a camera was effective for measuring optically trapped objects three-dimensionally [24]. A recently developed high-speed camera provided a temporal resolution comparable to that of a QPD [25]. Measuring the 3D position of trapped particles of

Multi-dimensional Imaging, First Edition. Edited by Bahram Javidi, Enrique Tajahuerce and Pedro Andrés.

micrometer-order diameters was demonstrated using a holographic method [26]. Three-dimensional position measurement was also demonstrated by using stereomicroscopy [27]. The Brownian motion of a polystyrene sphere with a 0.8 μm diameter was measured with a digital holographic microscope, although this technique did not use optical tweezers [28]. Despite these numerous studies, there has been little research into measuring the 3D position of subwavelength-sized particles (nanoparticles) with diameters smaller than the focal spot diameter used in optical tweezers techniques.

Recently, we demonstrated digital holographic measurement of a nanoparticle's position held in optical tweezers [29,30]. The diameter was smaller than that of nanoparticles used in previous studies [26–28]. The optical tweezers suppressed the movement of the nanoparticle and controlled its position in the use of a measurement probe. Digital holography [31] has been used to detect particles with no relation to optical tweezers [32–34]. Digital focusing on to an object was performed by a pattern matching between a diffraction image and a template image [29], but it has been performed by using features of the focused image, such as an iterative gradient computation [35], the maximization of the intensity local changes [36], a correlation coefficient [37], the sparsity of wavelet coefficients [38], and an integrated amplitude modulus [39,40]. An in-line digital holography setup can be also used for detecting the positions of particles [31,41,42]. In the system, in addition to an in-line digital holography setup, low-coherence light [41,43,44] was used to measure a nanoparticle, because the scattered light from the nanoparticle was very weak and was buried in speckles produced by unwanted scattered light.

The optical tweezers have been applied to manipulate gold nanoparticles when the motion, state, and function of a biological system are measured. The 3D trapping of the gold nanoparticle with a 36 nm diameter was first demonstrated by Svoboda and Block [6]. The optically trapped gold nanoparticle was used as a probe tip of a near-field optical microscope [45–47]. The heat effect of the optically trapped gold nanoparticle has also been discussed [48]. The stable optical trapping of 18–254 nm gold particles has been demonstrated [49]. Optical trappings of silver nanoparticles [50] and gold nanorods [51] has also been demonstrated. Theoretical calculations of the optical trapping force of the metal nanoparticles were described [52–54]. A gold nanoparticle with a 9.5 nm diameter [55] has been successfully trapped in optical tweezers and detected with a quadrant photodiode (QPD) method. These holographic methods were also applied to measure the position of the gold nanoparticle with the heterodyne technique [56,57] and the dark field arrangement [58].

In this chapter, position measurement of an optically trapped nanoparticle using low-coherence, inline-digital holography with a pattern matching method, and a 3D sub-pixel estimation is described. In Section 8.2, the optical setup, the image processing procedure, and sample preparation are described. In Section 8.3, the measurement accuracy of the experimental setup and the experimental results of measuring the Brownian motion of a polystyrene particle with diameters of 200 and 500 nm, while changing the trapping laser power and the 3D position measurement of a gold nanoparticle with 60 nm a diameter, is also demonstrated. In Section 8.4, a method for achieving higher accuracy in 3D position measurement of nanoparticles, using an in-line digital holographic microscope by increasing weak scattered light from a nanoparticle relative to the reference light with a low spatial frequency attenuation filter, is described [59]. In Section 8.5, some concluding remarks are presented.

8.2 Experimental Setup

8.2.1 Optical Tweezers System

Figure 8.1 shows the experimental setup, composed of an optical tweezers system and a low-coherence, in-line digital holographic microscope. This system was placed on a vibration isolation optical table. In the optical tweezers system, a beam generated from an Yb-fiber laser with a wavelength of 1070 nm (IPG Photonics, YLM-10) was collimated and focused in a sample solution using a 60× oil-immersion microscope objective lens (OL) with a numerical aperture of $NA = 1.25$. The irradiation laser power at the sample was controlled with a half-wave plate and a polarization beam splitter (PBS) and calculated as the product of the power measured before introducing the laser beam and the transmittance of the OL.

The samples were suspensions of polystyrene beads (diameter = 202 nm, standard deviation = 10 nm, 2.66% solid suspension, Polysciences, Inc.) diluted 1:48000 with distilled water, polystyrene beads (diameter = 535 nm, standard deviation = 10 nm, 2.69% solids suspension, Polysciences, Inc.) diluted 1:2500 with distilled water, and gold nanoparticles (diameter = 60 nm, 10% deviation, Tanaka Precision Metals) diluted 1:5000 in distilled water.

8.2.2 In-Line Digital Holographic Microscope

8.2.2.1 Optical Setup

In the in-line digital holographic microscope, the light source was a green light emitting diode (LED) (Luxeon, Green Revel Star/O) with a center wavelength of $\lambda_c = 528$ nm and a

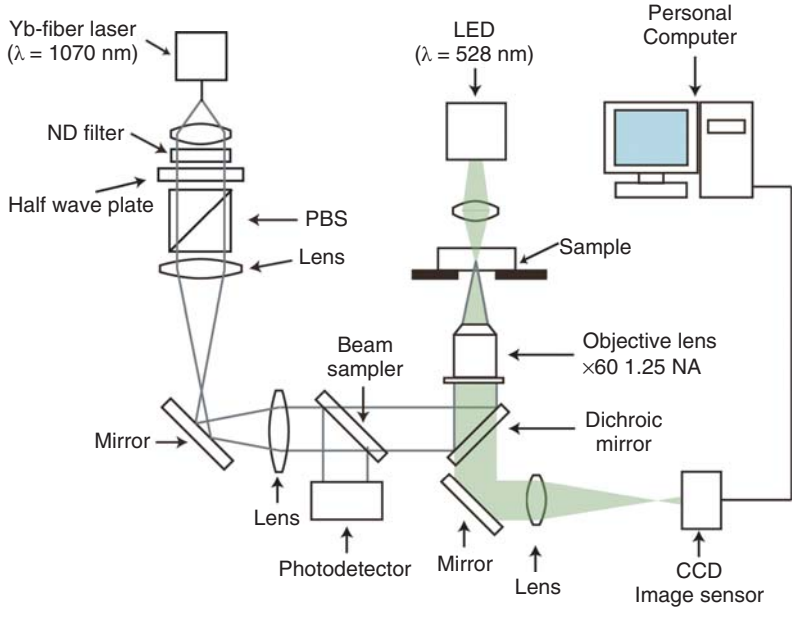

Figure 8.1 Experimental setup

spectral width of $\Delta\lambda = 32$ nm at the full-width half maximum. The green light was focused to obtain stronger illumination with the power of ~6 mW on the sample. The scattered light from a nanoparticle (the object light) and the straight-through light (the reference light) were magnified by the OL and a lens with a focal length of 300 mm, and interfered on a cooled charge-coupled device (CCD) image sensor (Bitran, BU50LN) with 772 × 580 pixels, 16-bit resolution, 1.0 ms shutter speed and 8.6 frames/s (fps). The diffraction limit and the Rayleigh length of the microscope calculated from λ_c and *NA* were $0.61\lambda_c/NA = 258$ nm and $\lambda_c/NA^2 = 338$ nm, respectively.

The lateral and axial magnifications of the in-line digital holographic microscope were estimated as follows. In the estimation of the lateral magnification, a 10.0 µm scale bar on the sample plane was measured as 121 pixels on the CCD image sensor, with a pixel spacing of 8.3 µm; therefore the lateral magnification M_L was 1.0×10^2. The corresponding spatial sampling interval on the sample plane was $\Delta x = \Delta y = 83$ nm. The axial magnification was estimated by the ratio of the displacements along the axial direction between the object plane and the image plane. In more detail, a 200 nm polystyrene particle fixed on a slide glass was axially moved between 0 and 4000 nm in steps of 500 nm, and the CCD image sensor was moved to the focused point (dark spot). The step of 500 nm along the axial movement of the sample corresponded to the axial movement of 3.9 mm in the focus position of CCD image sensor. Therefore the axial magnification was $M_A = 3.9\,\text{mm}/500\,\text{nm} = 7.8 \times 10^3$. For example, the axial step of 10 µm in the diffraction calculation on the image space corresponded to $\Delta z = 1.3$ nm in the sample space.

8.2.2.2 Diffraction Calculation

In the in-line digital holographic microscope, there was a short path difference between the object light and the reference light, allowing interference between them with low-coherence light. The interference image, $|u_k(x, y, z)|^2$, for wave-number $k = 2\pi/\lambda$ is approximated by the interference between a spherical wave from a point source (scattered light from nanoparticle) and a plane wave (straight-through light):

$$\begin{aligned}\left|u_k(x,y,z)\right|^2 &= \left|A_k^{(r)}\exp(ikz) + \frac{A_k^{(s)}}{\sqrt{x^2+y^2}}\exp\left(ik\frac{x^2+y^2}{2z}\right)\right|^2 \\ &= A_k^{(r)2} + \frac{A_k^{(s)2}}{x^2+y^2} + \frac{2A_k^{(r)}A_k^{(s)}}{\sqrt{x^2+y^2}}\cos k\left(z - \frac{x^2+y^2}{2z}\right)\end{aligned} \tag{8.1}$$

where $A_k^{(r)}$ and $A_k^{(s)}$ are the amplitudes of the straight-through light and scattered light, respectively. The scattered light from a nanoparticle is very weak [60,61]. Therefore, it will be lost among speckle noise if a high coherence light source such as a laser is used. When a broadband (low-coherence) light source is used, the interference image is described as

$$I_h(x,y,z) = \int_k \left|u_k(x,y,z)\right|^2 dk. \tag{8.2}$$

From the interference pattern, the diffraction calculation was performed on the basis of the angular spectrum method [62]. The object was a single nanoparticle, which was a very

simple object, so that the amplitude of the captured interference image was given by the amplitude-only hologram with a constant phase. The complex amplitude of a diffraction image $u(x, y, z)$ at the axial position z from a hologram $u_h(x, y, z_m)$ obtained at an axial position z_m is described as

$$u(x,y,z) = F_t^{-1}\left(F_t\left[u_h\left(x,y,z_m\right)\right]\exp\left[-2\pi i\sqrt{\lambda^{-2}-{\nu_x}^2-{\nu_y}^2}\left(z-z_m\right)\right]\right), \tag{8.3}$$

where ν_x and ν_y are the 2D coordinates of the spatial frequency plane, F_t and F_t^{-1} are the 2D Fourier transform in the transverse directions and the inverse transform, respectively.

Figure 8.2 shows the flowchart of the procedure for 3D position measurement of the nanoparticle, performed on a computer. First, N holograms were captured at a fixed time interval Δt. The diffraction calculation of each hologram was performed on $z = z_t + n_z\Delta z$ ($n_z = -N_z/2$, $-N_z/2+1$, … $N_z/2-1$), where z_t was an axial position where a template image was obtained and N_z was the number of diffraction calculations per hologram. $N_z = R_Z/\Delta z$, where R_Z was a measurement axial range. This number was closely related to the total calculation time, because the diffraction calculation was the biggest computational load in the calculation. $R_Z = 1.95\,\mu m$, which was larger than the movement of the trapped nanoparticle in each frame, was given.

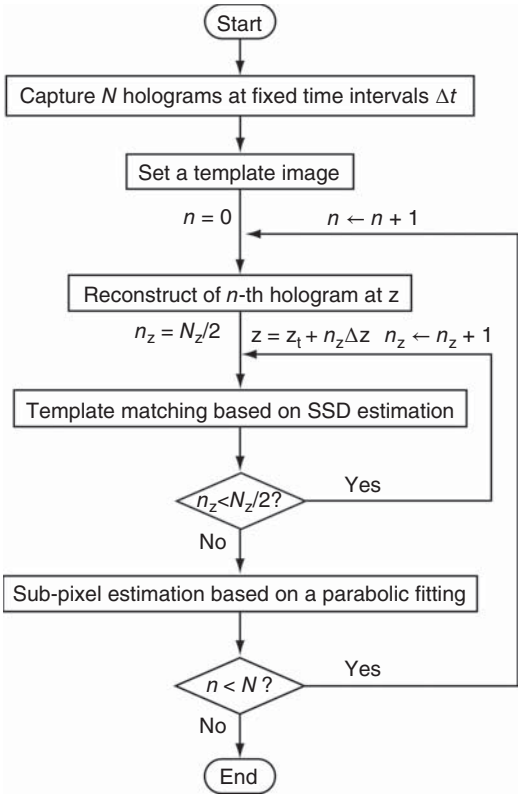

Figure 8.2 Flow chart

8.2.2.3 Template Matching

Template matching searches a 3D position that minimizes the sum of squared differences (SSD) between a diffraction image $I(x, y, z)$ and a template image $T(\xi, \zeta, z_0)$ that was previously set as the diffraction image where a nanoparticle was located at z_0. $I(x, y, z)$ is a diffraction image with $L \times L$ pixels, $T(\xi, \zeta, z_0)$ at the axial position z_0 is a template image with $M \times M$ pixels, and the SSD map is given by

$$SSD(x, y, z) = \sum_{\zeta=0}^{M-1} \sum_{\xi=0}^{M-1} \{I(x + \xi\Delta x, y + \zeta\Delta y, z) - T(\xi\Delta x, \zeta\Delta y, z_0)\}^2. \tag{8.4}$$

The minimum SSD value, $SSD_0 = SSD(x_{\min}, y_{\min}, z_{\min})$, was sought while changing x, y, and z from N_z diffraction images of the hologram obtained at a time t and the position ($x_{\min}$, $y_{\min}$, $z_{\min}$) was obtained. The lateral search region was restricted by $|x_n - x_{n-1}| < p\Delta x$ and $|y_n - y_{n-1}| < p\Delta y$, where $p = q = 25$, for reducing the calculation time.

Figure 8.3(a) shows an interference image $I(x, y, z)$ (a hologram of the 200 nm polystyrene particle). The image was clipped in a 51×51 pixel area around the position of the nanoparticle. Figures 8.3(b) and 8.3(c) show the diffraction images $I(x, y, z)$ at planes $z = -689$ nm and -1300 nm, respectively. Figure 8.3(d) shows the template image with 11×11 pixels $T(\xi, \zeta, z_0)$. The position that had the minimum amplitude was selected as the position of the nanoparticle from the diffraction image of the hologram obtained at $t = 0.00$s, in this case, from Fig. 8.3(b).

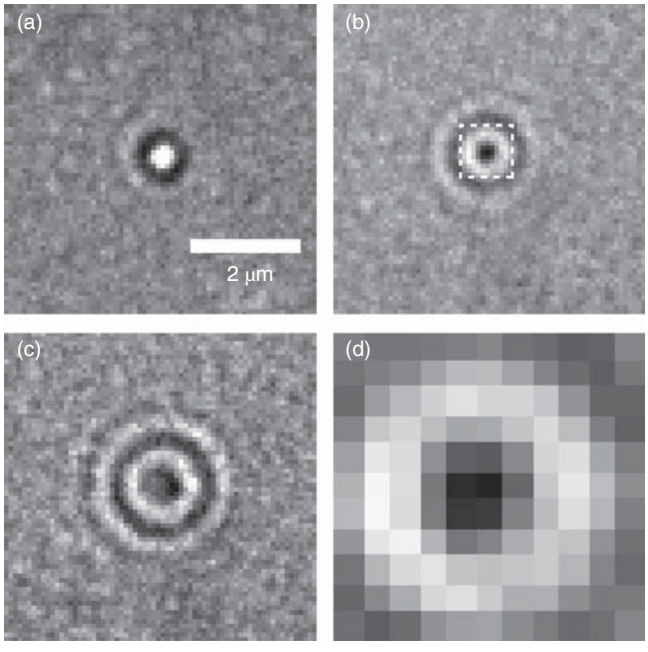

Figure 8.3 (a) Hologram of a polystyrene particle with a diameter of 200 nm and (b), (c) its diffraction images at distances $z = -689$ and -1300 nm. The square indicated in the dashed lines in (b) is clipped as the template in (d)

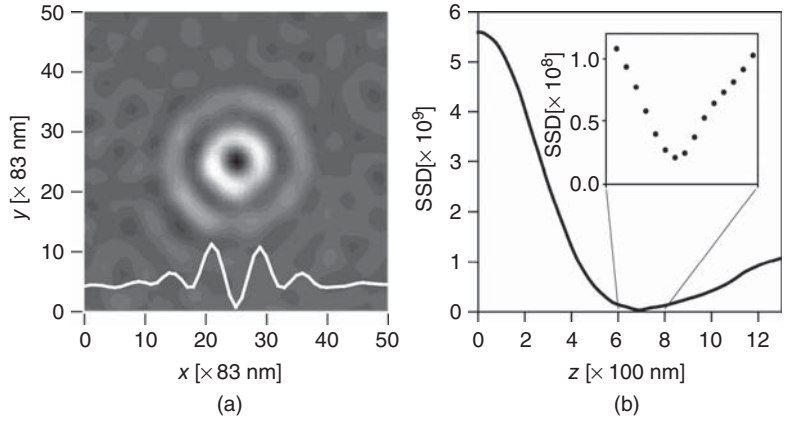

Figure 8.4 (a) The lateral SSD map and the profile through the center line including the minimum SSD. (b) The axial SSD profile. The inset shows a magnified view around the minimum SSD

This was selected experimentally, but optimization of the selection depending on the size and shape of the target object is important for improving the axial resolution. The size of the dark spot was 309 nm full width at half maximum (FWHM), which was slightly larger than the Airy disk diameter of 219 nm at FWHM. It means that the resolution of the holographic microscope was nearly equal to the theoretical resolution limit. The dashed square indicates the area clipped as $T(\xi, \zeta, z_0)$ from Fig. 8.3(b).

Figure 8.4(a) shows a lateral SSD map calculated from the diffraction image on the focus plane at $t = 1.17$s and the template image (Fig. 8.3d). It contained the point that had SSD_0, and the profile indicated by a white curve was obtained on the line that included SSD_0. Figure 8.4(b) shows the axial SSD profile at the position $(x_{\min}, y_{\min})$ and the inset shows a magnified view around $z_{\min}$.

8.2.2.4 Three-Dimensional Sub-Pixel Estimation

The sub-pixel estimation [30] was performed using parabolic fitting in the respective three-dimensional axes (see Fig. 8.4). From the SSD obtained in the template matching, the sub-pixel position x_{sub} was estimated from

$$x_{\text{sub}} = x_{\min} + \Delta x \frac{SSD_{-1} - SSD_1}{2SSD_{-1} - 4SSD_0 - 2SSD_1}. \tag{8.5}$$

where $SSD_{\text{n}} = SSD(x_{\min} + n\Delta x, y_{\min}, z_{\min})$. Same calculations were performed in the y and z directions to obtain the sub-pixel positions y_{sub} and z_{sub}, and the position of the nanoparticle was estimated as $(x_{\text{sub}}, y_{\text{sub}}, z_{\text{sub}})$. The movement of the nanoparticle was measured by performing the previous procedure for all holograms. In the 2D sub-pixel estimation, the calculations in Eq. (8.5) were performed only for the x and y directions [29], then the axial resolution was improved by minimizing Δz. The axial sub-pixel estimation drastically decreased the value of the diffraction calculation.

8.3 Experimental Results of 3D Position Measurement of Nanoparticles

8.3.1 A 200 nm Polystyrene Particle Fixed on a Glass Substrate

The accuracy of the 3D position measurement was estimated using a 200 nm polystyrene particle fixed on glass. Figure 8.5(a) shows the temporal changes for the measured positions of the fixed particle using the 3D sub-pixel estimation with $\Delta z = 13$ nm. The SDs of the temporal changes (the noise levels) for the x, y, and z directions were 3.5, 3.4, and 3.2 nm, respectively. These were much smaller than the diffraction limit and the Rayleigh length of the microscope and were smaller than the reported SDs measured with a high-speed camera and a QPD.

The system has three species of noises: optical noise, optoelectronic noise, and mechanical noise. The optical noise is an interference noise mainly caused by pollution on the optics. This was almost constant in this system. The optoelectronic noise mainly generated on the image sensor is temporally random. The main components of the mechanical noise were low frequency components because the vibration-isolation optical table eliminated the high frequency components that come from an external source. Therefore, the high frequency fluctuation in Fig. 8.5(a) was mainly caused by the optoelectronic noise. The thick gray curve

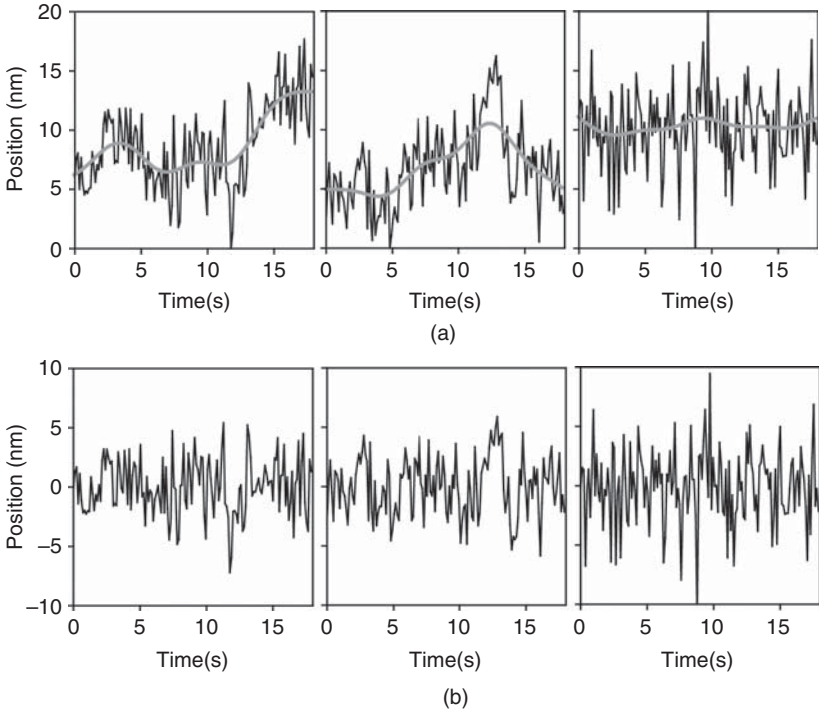

Figure 8.5 (a) 3D position measurement of a 200 nm polystyrene particle fixed on a glass substrate. The gray curves indicate the low frequency components of the temporal traces extracted by the low-pass filter based on the FFT. (b) The high frequency components that subtracted the low frequency components from the original temporal traces of the position measurements

indicates the low frequency components less than 0.3 Hz extracted by the low-pass filtering based on the FFT. Their SDs for the x, y, and z directions were 2.2, 2.0, and 0.4 nm, respectively. Figure 8.5(b) shows the high frequency components that subtracted the low frequency components from the original signals. The SDs for the x, y, and z directions were 2.3, 2.5, and 3.1 nm, respectively. The low frequency components had smaller values in the z-direction than in the x- and y-directions, and the high frequency components had larger values in the z-direction than in x- and y-directions.

8.3.2 Axial Step in 3D Sub-Pixel Estimation

To increase the axial step Δz in the 3D sub-pixel estimation leads to a decrease in the computational cost of the diffraction calculation that is the biggest load in 3D position measurement. Figure 8.6 shows the measurement error for the axial step in the sub-pixel estimation. The filled circles indicate the results of the 3D sub-pixel estimation. For comparison, the results of the 2D sub-pixel estimation without the axial sub-pixel estimation are indicated by the open circles. The circles on the solid curves indicate the SDs of the measured axial position, described as

$$SD_z = \sqrt{\frac{1}{N}\sum_{n=1}^{N}\left(z_{sub}(n) - \overline{z_{sub}}\right)^2}, \tag{8.6}$$

where $\overline{z_{sub}}$ is the mean value of $z_{sub}(n)$. This well-known equation is noted here for easily understanding comparison with the next equation. For 2D sub-pixel estimation, $z_{\min}(n)$ and $\overline{z_{\min}}$ were used instead of $z_{sub}(n)$ and $\overline{z_{sub}}$ in the calculations.

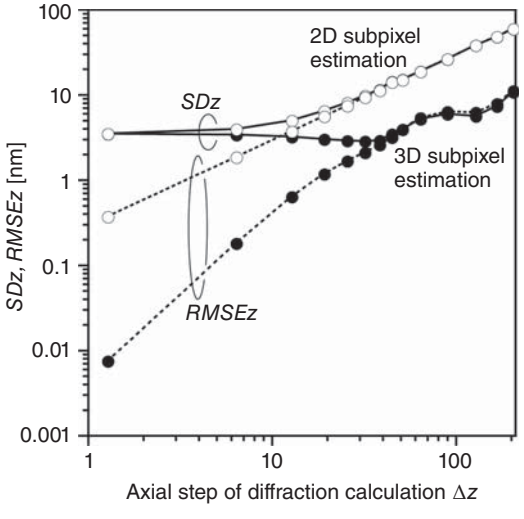

Figure 8.6 SD_z and $RMSE_z$ of the position measurements of the fixed particle for Δz. The open and the filled circles indicate the 2D and 3D sub-pixel estimations, respectively. The solid and dashed curves indicate SD_z and $RMSE_z$, respectively

The circles on the dashed curves indicate the root mean square error (RMSE) of the measured axial position $z_{\min}(n)|_{\Delta z=0.13\,\mathrm{nm}}$, which is the most probable value of the true position when the minimum $\Delta z = 0.13$ nm was given and the 2D sub-pixel estimation was performed, given by

$$RMSE_z = \sqrt{\frac{1}{N}\sum_{n=1}^{N}(z_{sub}(n) - z_{\min}(n)|_{\Delta z=0.13\,\mathrm{nm}})^2}. \tag{8.7}$$

Similarly, $z_{\min}(n)$ was used instead of $z_{sub}(n)$ for 2D sub-pixel estimation.

First, the results of the 2D and 3D sub-pixel estimations were compared. The 3D sub-pixel estimation had smaller errors than the 2D sub-pixel estimation for any Δz. When $\Delta z < \sim 40$ nm, SD_z of the 3D sub-pixel estimation reached the lower limit of ~3 nm. SD_z represented the system resolution, which was determined by the SNR of the interference fringes, the SNR of image sensor noise, and mechanical stability of the optical system, as described before.

$RMSE_z$ was free from the optical, optoelectronic, and mechanical noises, which determined the system resolution. $RMSE_z$ depended only on the axial step Δz in the diffraction calculation; therefore, it decreased with a smaller Δz, which got near to the sufficiently small value of 0.13 in this study. In the 2D sub-pixel estimation, $RMSE_z$ had a linear dependence for Δz because it was caused by quantization error. In the 3D sub-pixel estimation, a quadratic dependence was observed when $\Delta z < 10$ nm because parabola fitting was used, and the axial profile of SSD was sufficiently fitted with the parabola function. When $\Delta z > 30$ nm, $RMSE_z$ showed a complex curve because the axial profile of SSD was different from the parabola function (see Fig. 8.4b) and the dependencies departed from the parabola function with increasing Δz.

8.3.3 Brownian Motion of a 200 nm Polystyrene Particle Held in Optical Tweezers

Figure 8.7 (Plate 14) shows the 3D positions of a 200 nm polystyrene particle exhibiting Brownian motion in the trapping volume of the optical tweezers. The traveling direction of the laser beam was from the bottom to the top of the graph and the gravity direction was the reverse. The holograms were recorded at 8.6 fps. The laser intensities were $I = 4.4$, 5.6, and 14.8 MW/cm^2, respectively. With the increase of laser intensity, the Brownian motion was reduced. Figure 8.8 shows the change in Brownian motion in response to changing the trapping laser power. The Brownian motion of the 200 nm particle changed drastically when $I < 14.8$ MW/cm^2. When $I < 4.4$ MW/cm^2, the Brownian motion was too strenuous and the particle was trapped for only a few seconds. When $I > 18.7$ MW/cm^2, the particle showed movement of less than two times greater than the noise level: that is, almost motionless. Similarly, the Brownian motion of a 500 nm particle became large when $I < 0.15$ MW/cm^2, and was almost completely motionless when $I > 0.97$ MW/cm^2. Here, we define the threshold power of the optical trapping as the smallest I where a particle was trapped over a long time. The threshold intensities for the 200 and 500 nm polystyrene particles were 4.4 and 0.53 MW/cm^2, respectively. This method is very useful for determining the threshold intensity of optical trapping and the 3D directional property.

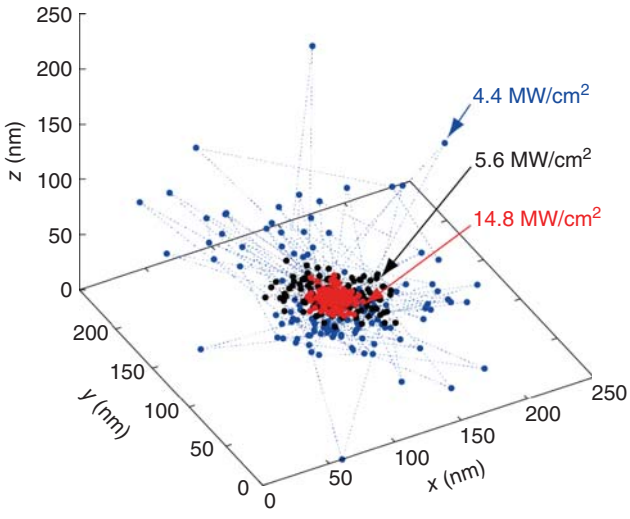

Figure 8.7 (Plate 14) Movement of a 200 nm polystyrene particle in the trapping volume at different intensities: (blue) 4.4 MW/cm^2, (black) 5.6 MW/cm^2, and (red) 14.8 MW/cm^2. *See plate section for the color version*

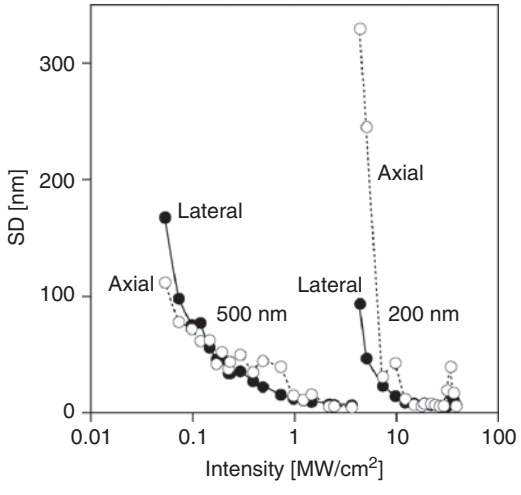

Figure 8.8 Change in Brownian motion with a change of the trapping laser intensity. The particles' diameters are 200 and 500 nm. The filled and open circles indicate the SDs of the lateral and axial movements, respectively

8.3.4 *Brownian Motion of a 60 nm Gold Nanoparticle Held in Optical Tweezers*

Figure 8.9 shows the measured 3D position of the optically trapped gold nanoparticle with a diameter of 60 nm. The detectable axial range roughly estimated from the 3D movement of gold nanoparticle was 1200 nm (from +900 to −300 nm from the trapping point) (see Fig. 8.10 (Plate 15)). When the laser intensity was 5.6 MW/cm^2 (Fig. 8.9a), the gold nanoparticle moved drastically according to the Brownian motion, especially in the axial direction because the axial force was lower than the lateral force. The axial movement was bigger toward the beam direction and the gold nanoparticle sometimes went off from the laser focus region to the axial upper direction (the beam direction) beyond the axial detectable region. The behavior was

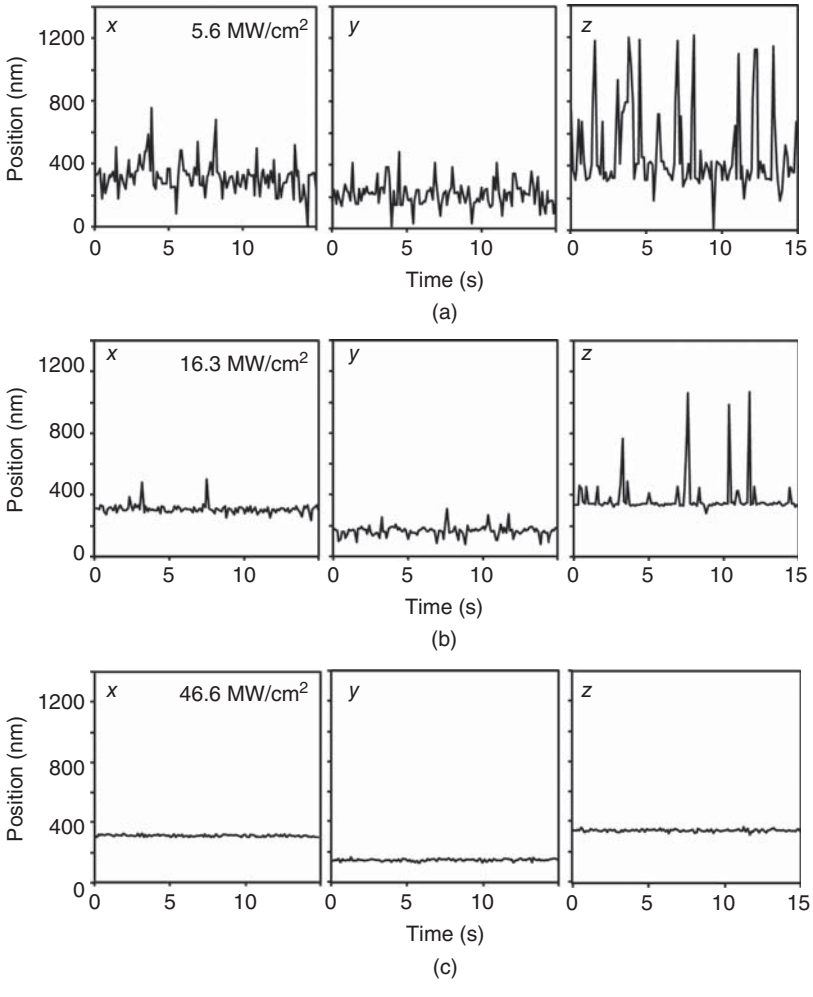

Figure 8.9 Three-dimensional position of a 60 nm gold nanoparticle trapped in optical tweezers with intensity of (a) $I = 5.6$ MW/cm^2, (b) 16.3 MW/cm^2, and (c) 46.6 MW/cm^2

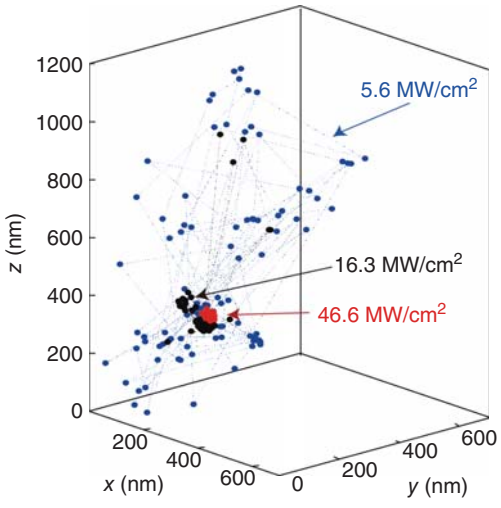

Figure 8.10 (Plate 15) Three-dimensional display of the gold nanoparticle movements. *See plate section for the color version*

different from that of a 200 nm polystyrene particle. It is dependent on the balance between the scattering force and the gradient force. The gradient force for a gold nanoparticle is much smaller than the scattering force. With an increase in laser intensity (Figs. 8.9b and 8.9c), the movement was reduced. When the laser intensity was 46.6 MW/cm^2, the gold nanoparticle was almost fixed and the lateral and axial variations were 6.1 and 7.1 nm, respectively. The spatial resolutions were a little lower than those of a 200 nm polystyrene particle.

Figure 8.11 shows the Brownian motion in response to changing the trapping laser intensity. The motion of the gold nanoparticle became bigger with the intensity smaller

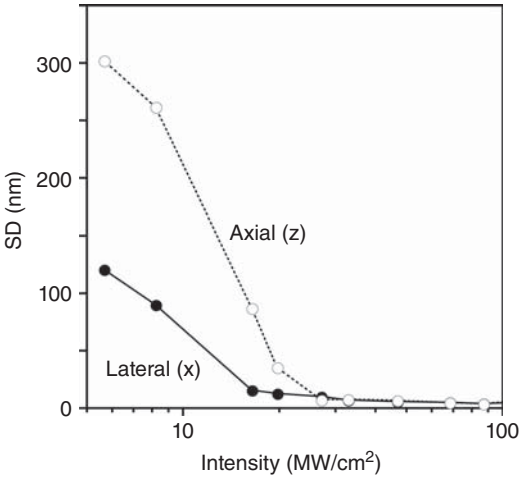

Figure 8.11 Brownian motion of a 60 nm gold nanoparticle dependent on the trapping laser intensity

than $I < 20\,\mathrm{MW/cm^2}$. When $I = 5.6\,\mathrm{MW/cm^2}$, the change was too strenuous, and the gold nanoparticle went off sometimes and returned back to the trapping region. When $I < 5.6\,\mathrm{MW/cm^2}$, the gold nanoparticle went off for a long time and did not return. Here, we define the threshold intensity of the optical trapping of a 60 nm gold nanoparticle under this laser focusing conditions as the smallest I where a particle was trapped over a long time period. When $I > 30\,\mathrm{MW/cm^2}$, the gold nanoparticle was almost completely motionless. The SDs of the measurement variations along the lateral and axial directions were 6.3 and 7.1 nm, respectively. When $I < 20\,\mathrm{MW/cm^2}$, the larger variation for smaller nanoparticle depended on the Brownian motion. When $I > 20\,\mathrm{MW/cm^2}$, the Brownian motion was suppressed and the random signals were caused only by noises in the measurement system.

8.4 Twilight Field Technique for Holographic Position Detection of Nanoparticles

8.4.1 Twilight Field Optical Microscope

When a nanoparticle of a much smaller size is used as a target, the quality of interference fringes is greatly decreased because of the ultra-weak scattered light intensity, and as a result, the accuracy of 3D measurement is decreased. A method for obtaining interference fringes, with higher signal-to-noise ratios (SNR) of amplitude in the 3D position measurement of a nanoparticle by using an in-line digital holographic microscope, is described in this section. The key component in the method is a low-frequency attenuation filter (LFAF) that only reduces the intensity of the reference light, which is non-scattered straight-through light, close to the intensity of the object light from one of the nanoparticles. When the LFAF has a transmittance of 1, the digital holographic microscope works as an ordinary bright field; conversely when the LFAF has a transmittance close to 0, it works like a dark field microscope. This method uses the intermediate transmittance, that is, the intermediate between bright field and dark field. Therefore, the proposed system is called a *twilight field optical microscope* [59].

When a nanoparticle with a radius r and a refractive index n_1 surrounded by a solution with a refractive index n_0 is in an in-line DHM, the angular distribution of the scattered light intensity at a distance d with respect to incident light intensity I_{inc} with wave-number k is given by the well-known Rayleigh scattering theory:

$$I_{sca}(\theta, d) = \frac{k^4 r^6}{d^2}\left(\frac{m^2-1}{m^2+1}\right)\left(\frac{1+\cos^2\theta}{2}\right) I_{inc} = \alpha(\theta, d) I_{inc}, \tag{8.8}$$

where $m = n_1/n_0$ and α is a scattering coefficient depending on the angle θ and the distance d. This equation shows that I_{sca} decreases with the sixth power of r. The interference signal I between the scattered light and the straight-through reference light I_{ref} is described as

$$I = I_{ref} + I_{sca} + 2\sqrt{I_{ref} I_{sca}}\cos(\theta) + N, \tag{8.9}$$

where θ is a phase, N represents a magnitude of optical and optoelectronic noises. From Eq. (8.8), for a nanoparticle $I_{sca} \ll I_{inc}$: So $I_{ref} \approx I_{inc}$. *SNR* of the fringes, which is defined as the fringe amplitude $2(I_{ref} I_{sca})^{1/2}$ divided by N, is given by

$$SNR = \frac{2\sqrt{I_{ref} I_{sca}}}{N} \approx \frac{2I_{inc}\sqrt{\alpha}}{N} \approx \frac{2I_{ref}\sqrt{\alpha}}{N}. \tag{8.10}$$

From Eq. (8.10), it can be seen that the *SNR* can be increased by decreasing N and increasing α. N can be decreased by using an image sensor with small noise and by reducing undesired interference (speckle noise). α can be increased by using a light source with a large wave-number. Once these improvements have been realized for a certain application, the *SNR* can be increased only by increasing I_{inc}. However, the increase of I_{inc} is limited by the maximum detectable value of the image sensor, denoted as $I_{\max}$. Consequently, the *SNR* has an upper limit according to the nanoparticle's physical properties, after selecting the system components.

Now it is assumed that I_{ref} at the plane after light scattering from the nanoparticle is decreased by the LFAF with a transmittance of T_{R}, and I_{inc} is increased by a factor of $g(>1)$. The interference signal is

$$I = gT_{\mathrm{R}}I_{ref} + gI_{sca} + 2g\sqrt{T_{\mathrm{R}}I_{ref}I_{sca}}\cos(\theta) + N. \tag{8.11}$$

If $T_{\mathrm{R}}I_{ref} \gg I_{sca}$ and g is regulated to satisfy the condition $gT_{\mathrm{R}} = 1$, technically speaking, the condition $I < I_{\max}$ is always satisfied, the optical noise, which is directly proportional to the intensity of the light falling onto the image sensor is retained, and so the *SNR* increases in proportion to ${T_{\mathrm{R}}}^{-1/2}$, as indicated in Eq. (8.12). This equation shows that it is possible to obtain an arbitrary value of the *SNR* by using an LFAF with appropriate design, that is, with an appropriate T_{R}, as described by:

$$SNR \approx \frac{2I_{inc}\sqrt{\alpha/T_R}}{N}. \tag{8.12}$$

From this equation, the highest *SNR* is obtained under $\alpha = T_{\mathrm{R}}$, however, then a very strong light source satisfying $gT_{\mathrm{R}} = 1$ is required. In practice, T_{R} uses the full dynamic range of the image sensor with dependence on the light source intensity and an acceptable intensity to the sample.

8.4.2 Low-Coherence, In-Line Digital Holographic Microscope with the LFAF

A low-coherence, in-line digital holographic microscope with the LFAF is shown in Fig. 8.12. The light source was an optical fiber coupled with a light emitting diode (LED), a center wavelength of 450 nm, and a spectral width of 25 nm. The light was focused near the sample to obtain strong illumination. The sample was a 100 nm-diameter polystyrene particle in water, sandwiched by a slide glass and a cover glass. The light scattered from the nanoparticle and the non-scattered reference light was magnified by a 60× objective lens (1.25NA) and lenses

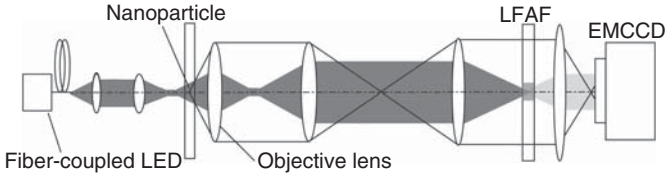

Figure 8.12 In-line digital holographic microscope with LFAF

through the LFAF. The LFAF had a simple structure, made of a thin transparent film with a semi-transparent circle of a 1 mm diameter. The interference fringes were detected by an electron-multiplying CCD (EMCCD) image sensor (DU-888, Andor) with a low noise and a frame interval of 29.6 ms. The captured interference images were reconstructed based on the angular spectrum method on a computer. The axial magnification M_a was $M_a = 5.1 \times 10^3$. The diffraction image was calculated according to the propagation distance z, which was scanned in the maximum movement range of the nanoparticle at intervals of $\Delta z = 0.1$ nm. Image processing was performed, including the pattern matching and the subpixel display, but only in the transverse directions, and was almost same as the method described in Section 8.2.2.

8.4.3 Improvement of Interference Fringes of a 100 nm Polystyrene Nanoparticle

Figure 8.13 shows the interference fringes of a 100 nm polystyrene nanoparticle fixed on the substrate glass, located at a position of $z = 1.5$ μm from the focal plane of the objective lens and captured (a) without the LFAF ($T_R = 1.0$), (b) with the LFAF ($T_R = 0.19$), and (c) with the LFAF ($T_R = 0.08$). These images show the increase in contrast of the interference fringes with the use of the denser LFAF. In the experiment, a standard environmental noise deviation of 10 counts/s was measured when the light source was blocked. The incident light intensity on the CCD image sensor was adjusted to an average intensity of 4.0×10^3 counts/s, and it was kept the same during the experiment in both cases, with and without the LFAF.

Figure 8.14(a) shows *SNR* of the fringes as a function of ${T_R}^{-1/2}$. The filled and open circles indicate the results when the nanoparticle positions were $z = 1.5$ and 3.0 μm from the focal plane, respectively. The contrast of the interference fringes was calculated from the maximum and minimum intensities of the circular fringes, which were respectively measured from the center dark spot and the surrounding bright ring in the diffraction image of the hologram. *SNR* was improved by using the LFAF and increasing I_{inc}. As theoretically expected from Eq. (8.11), *SNR* was proportional to ${T_R}^{-1/2}$ because of $\alpha/T_R \ll 1$ in this experiment. The 3D positions of a 100 nm particle were obtained from 100 holograms, and the standard deviations σ_x, σ_y, and σ_z along the x, y, and z directions were calculated to evaluate the accuracy of the measurement. Figures 8.14(b) and 8.14(c) show σ_y and σ_z as functions of ${T_R}^{-1/2}$, respectively. Here, σ_x is not shown because it was similar to σ_y. The improvement in *SNR* that was realized by using the dense LFAF increased the accuracy of the 3D position measurement of the nanoparticle.

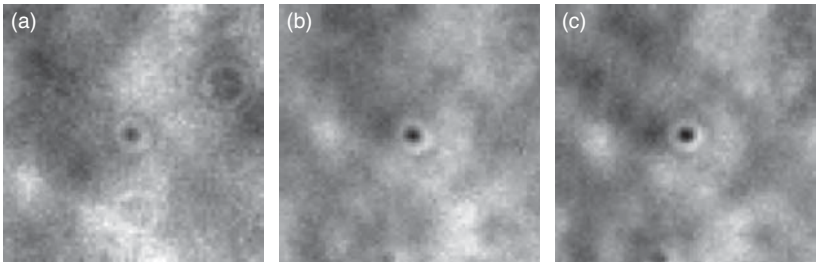

Figure 8.13 Holographic images of nanoparticle captured (a) without the LFAF ($T_R = 1.0$), (b) with the LFAF ($T_R = 0.19$), and (c) with the LFAF ($T_R = 0.08$)

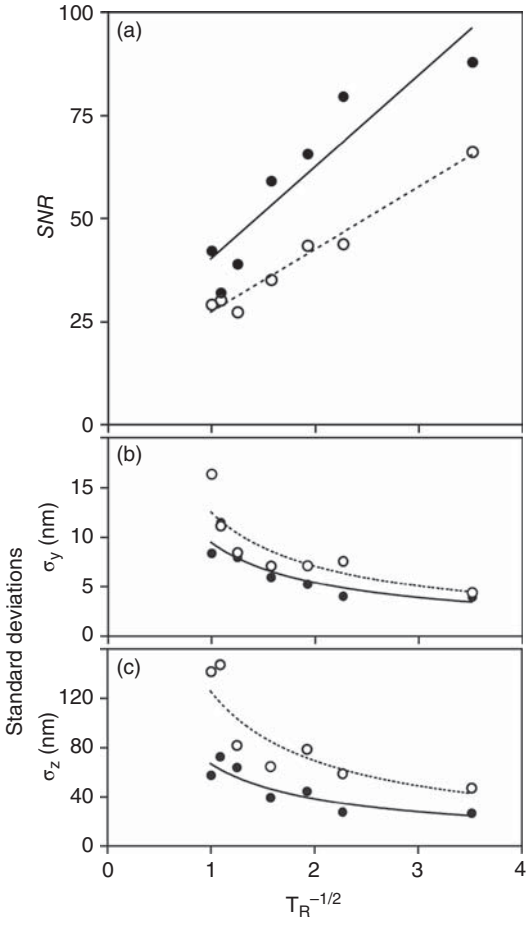

Figure 8.14 (a) *SNR* as a function of $T_R^{-1/2}$ under constant reference light intensity. Standard deviations along the (b) *y*- and (c) *z*-directions as a function of $T_R^{-1/2}$. The filled and open circles indicate the results when the nanoparticle positions were $z = 1.5$ and 3.0 μm from the focal plane, respectively

8.5 Conclusion

This chapter described a position measurement of an optically-trapped nanoparticle using a low-coherence, in-line digital holographic microscope, with the pattern matching method based on the SSD estimation and the 3D sub-pixel estimation of the SSD map. The optical setup, the image processing procedure, and sample preparation were described. The behaviors of the trapped nanoparticle and the spatial resolution of the microscope were demonstrated.

The 3D position measurement of a 200 nm polystyrene particle held by optical tweezers in water was demonstrated. The optical tweezers performed the 3D positioning of the 200 nm polystyrene particle in a volume smaller than ∼3 nm in SD, which corresponded to the noise level; that is, the spatial resolution of the holographic microscope. The lateral and

axial resolutions were obtained from the position measurements of a 200 nm polystyrene particle fixed on the glass substrate. They were much smaller than the diffraction limit and the Rayleigh length of the microscope, respectively. The movement of the 200 nm polystyrene particle trapped by the optical tweezers in water was measured. When $I > 18.7\,\mathrm{MW/cm^2}$, the particle had the movement of less than two times larger than the noise level; that is, almost motionless. The movement was compared with that of the 500 nm polystyrene particle. The results revealed that the threshold laser intensity for trapping the 200 and 500 nm particles were 4.4 and $0.53\,\mathrm{MW/cm^2}$, respectively.

The 3D position of a 60 nm gold particle held by optical tweezers in water was also measured. The threshold trapping intensity was $I = 5.6\,\mathrm{MW/cm^2}$ and the gold nanoparticle was almost fixed with $I > 30\,\mathrm{MW/cm^2}$. From the comparison of movements between a gold nanoparticle fixed on a glass substrate and fixed by optical tweezers with a sufficient optical trapping laser intensity, we analyzed the three kinds of noise; optical, optoelectronic, and mechanical.

This holographic method was a very powerful tool for detailed study of the threshold of optical trapping, especially the ability of 3D measurements to measure a directional property. The threshold intensity depends on not only the particle's property but also a relationship between a particle and its surroundings. The further study of the threshold will be very interesting. This system will be useful for 3D mechanical measurement using optically trapped nanoparticles in fluid and biological systems.

Toward the observation of a smaller particle using an in-line digital holographic microscope, the twilight field method based on increased illumination and use of a light attenuation filter at a low spatial frequency was developed. The method can overcome the limitations in conventional holographic measurement of nanoparticles. The method improved the quality of the interference fringes and the accuracy of 3D position measurement of a nanoparticle.

Finally, in this section, an optical tweezers method for positioning a nanoparticle, an in-line digital holographic microscope with some image processing methods for measuring a nanoparticle's position, and a method for obtaining higher quality interference fringes of a nanoparticle were proposed. Consequently, these useful methods could well be required for improvements in advanced microscopy. Nanoparticle technology is very promising for a variety of scientific and engineering fields in future, and 3D position measurement of nanoparticles will be very effective for them.

References

[1] Ashkin, A., J. M. Dziedzic, J. E. Bjorkholm, and S. Chu, "Observation of a single-beam gradient force optical trap for dielectric particles," *Opt. Lett.* **11**, 288–290 (1986).

[2] Ashkin, A. and J. M. Dziedzic, "Optical trapping and manipulation of viruses and bacteria," *Science* **235**, 1517–1520 (1987).

[3] Tinoco, Jr., I., D. Collin, and P. T. X. Li, "Unfolding single RNA molecules: bridging the gap between equilibrium and non-equilibrium statistical thermodynamics," *Q. Rev. Biophys.* **38**, 291–301 (2005).

[4] Neuman, K. C. and A. Nagy, "Single-molecule force spectroscopy: optical tweezers, magnetic tweezers and atomic force microscopy," *Nature Methods* **5**, 491–505 (2008).

[5] Ichikawa, M., Y. Matsuzawa, Y. Koyama, and K. Yoshikawa, "Molecular fabrication: aligning DNA molecules as building blocks," *Langmuir* **19**, 5444–5447 (2003).

[6] Svoboda, K., C. F. Schmidt, B. J. Schnapp and S. M. Block, "Direct observation of 18 kinesin stepping by optical trapping interferometry," *Nature* **365**, 721–727 (1993).

[7] Greenleaf, W. J. and S. M. Block, "Single-molecule, motion-based DNA sequencing using RNA polymerase," *Science* **313**, 801–803 (2006).
[8] MacDonald, M. P., G. C. Spalding, and K. Dholakia, "Microfluidic sorting in an optical lattice," *Nature* **426**, 421–424 (2003).
[9] Ladavac, K., K. Kasza, and D. G. Grier, "Sorting mesoscopic objects with periodic potential landscapes: optical fractionation," *Phys. Rev. E* **70**, 010901(R) (2004).
[10] Miyazaki, M. and Y. Hayasaki, "Motion control of low-index microspheres in liquid based on optical repulsive force of a focused beam array," *Opt. Lett.* **34**, 821–823 (2009).
[11] Nakanishi, S., S. Shoji, S, Kawata, and H.-B. Sun, "Giant elasticity of photopolymer nanowires," *Appl. Phys. Lett.* **91**, 063112 (2007).
[12] Eom, S. I., Y. Takaya, and T. Hayashi, "Novel contact probing method using single fiber optical trapping probe," *Prec. Eng.* **33**, 235–242 (2009).
[13] Dufresne, E. R. and D. G. Grier, "Optical tweezer arrays and optical substrates created with diffractive optical elements," *Rev. Sci. Instrum.* **69**, 1974–1977 (1998).
[14] Hayasaki, Y., M. Itoh, T. Yatagai, and N. Nishida, "Nonmechanical optical manipulation of microparticles using spatial light modulator," *Opt. Rev.* **6**, 24–27 (1999).
[15] Reicherter, M., T. Haist, E. U. Wagemann, and H. J. Tiziani, "Optical particle trapping with computer-generated holograms written on a liquid-crystal display," *Opt. Lett.* **24**, 608–610 (1999).
[16] Jordan, P., H. Clare, L. Flendrig, J. Leach, J. Cooper, and M. Padgett, "Permanent 3D microstructures in a polymeric host created using holographic optical tweezers," *J. Mod. Opt.* **51**, 627–632 (2004).
[17] Roichman, Y. and D. G. Grier, "Holographic assembly of quasicrystalline photonic heterostructures," *Opt. Express* **13**, 5434–5439 (2005).
[18] Agarwal, R., K. Ladavac, Y. Roichman, G. Yu, C. M. Lieber, and D. G. Grier, "Manipulation and assembly of nanowires with holographic optical traps," *Opt. Express* **13**, 8906–8912 (2005).
[19] Gittes, F. and C. F. Schmidt, "Interference model for back-focal-plane displacement detection in optical tweezers," *Opt. Lett.* **23**, 7–9 (1998).
[20] Pralle, A., M. Prummer, E. L. Florin, E. H. K. Stelzer, and J. K. H. Hörber, "Three-dimensional high-resolution particle tracking for optical tweezers by forward scattered light," *Microsc. Res. Tech.* **44**, 378–386 (1999).
[21] Meiners, J. S. and S. Quake, "Direct measurement of hydrodynamic cross correlations between two particles in an external potential," *Phys. Rev. Lett.* **82**, 2211–2214 (1999).
[22] Huisstede, J. H. G., K. O. van der Werf, M. L. Bennink, and V. Subramaniam, "Force detection in optical tweezers using backscattered light," *Opt. Express* **13**, 1113–1123 (2005).
[23] Tolic-Norrelykke, S. F., E. Schäffer, J, Howard, F. S. Pavone, F. Jülicher, and H. Flyvbjerg, "Calibration of optical tweezers with positional detection in the back focal plane," *Rev. Sci. Instrum.* **77**, 103101 (2006).
[24] Gibson, G. M., J. Leach, S. Keen, A. J. Wright, and M. J. Padgett, "Measuring the accuracy of particle position and force in optical tweezers using high-speed video microscopy," *Opt. Express* **16**, 14561–14570 (2008).
[25] Otto, O., C. Gutsche, F. Kremer, and U. F. Keyser, "Optical tweezers with 2.5 kHz bandwidth video detection for single-colloid electrophoresis," *Rev. Sci. Instrum.* **79**, 023710 (2008).
[26] Lee, S. H. and D. G. Grier, "Holographic microscopy of holographically trapped three-dimensional structures," *Opt. Express* **15**, 1505–1512 (2007).
[27] Bowman, R., G. Gibson, and M. Padgett, "Particle tracking stereomicroscopy in optical tweezers: control of trap shape," *Opt. Express* **18**, 11785–11790 (2010).
[28] Dixon, L., F. C. Cheong, and D. G. Grier, "Holographic deconvolution microscopy for high-resolution particle tracking," *Opt. Express* **19**, 16410–16417 (2011).
[29] Higuchi, T., Q. D. Pham, S. Hasegawa, and Y. Hayasaki, "Three-dimensional positioning of optically-trapped nanoparticles," *Appl. Opt.* **50**, H183–H188 (2011).

[30] Sato, A., Q. D. Pham, S. Hasegawa, and Y. Hayasaki, "Three-dimensional subpixel estimation in holographic position measurement of an optically trapped nanoparticle," *Appl. Opt.* **52**, A216–A222 (2013).
[31] Onural, L. and P. D. Scott, "Digital recording of in-line holograms," *Opt. Eng.* **26**, 1124–1132 (1987).
[32] Schnars, U. and W. Jüptner, "Direct recording of holograms by a CCD target and numerical reconstruction," *Appl. Opt.* **33**, 179–181 (1994).
[33] Skarman, B., K. Wozniac, and J. Becker, "Simultaneous 3D-PIV and temperature measurement using a new CCD based holographic interferometer," *Flow Meas. Instrum.* **7**, 1–6 (1996).
[34] Garcia-Sucerquia, J., W. Xu, S. K. Jericho, P. Klages, M. H. Jericho, and H. J. Kreuzer, "Digital in-line holographic microscopy," *Appl. Opt.* **45**, 836–850 (2006).
[35] Yu, L. and L. Cai, "Iterative algorithm with a constraint condition for numerical reconstruction of a three-dimensional object from its hologram," *J. Opt. Soc. Am. A* **18**, 1033–1045 (2001).
[36] Ma, L., H. Wang, Y. Li, and H. Jin, "Numerical reconstruction of digital holograms for three-dimensional shape measurement," *J. Opt. A* **6**, 396–400 (2004).
[37] Yang, Y., B. S. Kang, and Y. J. Choo, "Application of the correlation coefficient method for determination of the focus plane to digital particle holography," *Appl. Opt.* **47**, 817–824 (2008).
[38] Liebling, M. and M. Unser, "Autofocus for digital Fresnel holograms by use of a Fresnelet-sparsity criterion," *J. Opt. Soc. Am. A* **21**, 2424–2430 (2004).
[39] Dubois, F., C. Schockaert, N. Callens, and C. Yourassowski, "Focus plane detection criteria in digital holography microscopy by amplitude analysis," *Opt. Express* **14**, 5895–5908 (2006).
[40] Mallahi, E. and F. Dubois, "Dependency and precision of the refocusing criterion based on amplitude analysis in digital holographic microscopy," *Opt. Express* **19**, 6684–6698 (2011).
[41] Dubois, F., N. Callens, C. Yourassowsky, M. Hoyos, P. Kurowski, and O. Monnom, "Digital holographic microscopy with reduced spatial coherence for three dimensional particle flow analysis," *Appl. Opt.* **45**, 864–871 (2006).
[42] Cheong, F. C., B. J. Krishnatreya, and D. G. Grier, "Strategies for three-dimensional particle tracking with holographic video microscopy," *Opt. Express* **18**, 13563–13573 (2010).
[43] Pedrini, G. and H. J. Tiziani, "Short-coherence digital microscopy by use of a lensless holographic imaging system," *Appl. Opt.* **41**, 4489–4496 (2002).
[44] Tamano, S., Y. Hayasaki, and N. Nishida, "Phase-shifting digital holography with a low-coherence light source for reconstruction of a digital relief object hidden behind a light-scattering medium," *Appl. Opt.* **45**, 953–959 (2006).
[45] Sugiura, T., T. Okada, Y. Inouye, O. Nakamura, and S. Kawata, "Gold-bead scanning near-field optical microscope with laser-force position control," *Opt. Lett.* **22**, 1663–1665 (1997).
[46] Kalkbrenner, T., M. Ramstein, J. Mlynek, and V. Sandoghdar, "A single gold particle as a probe for apertureless scanning near-field optical microscopy," *J. Microscopy* **202**, 72–76 (2001).
[47] Ukita, H., H. Uemi, and A. HIrata, "Near field observation of a refractive index grating and a topologocal grating by an optically-trapped gold particle," *Opt. Rev.* **11**, 365–369 (2004).
[48] Seol, Y., A. E. Carpenter, and T. T. Perkins, "Gold nanoparticles: enhanced optical trapping and sensitivity coupled with significant heating," *Opt. Lett.* **31**, 2429–2431 (2006).
[49] Hansen, P. M., V. K. Bhatia, N. Harrit, and L. Oddershede, "Expanding the optical trapping range of gold nanoparticles," *Nano Lett.* **5**, 1937–1942 (2005).
[50] Bosanac L., T. Aabo, P. M. Bendix, and L. B. Oddershede, "Efficient optical trapping and visualization of silver nanoparticles," *Nano Lett.* **8**, 1486–1491 (2008).
[51] Selhuber-Unkel, C., I. Zins, O. Schubert, and C. Sönnichsen, L. B. Oddershede, "Quantitative optical trapping of single gold nanorods," *Nano Lett.* **8**, 2998–3003 (2008).
[52] Furukawa, H. and I. Yamaguchi, "Optical trapping of metallic particles by a fixed Gaussian beam," *Opt. Lett.* **23**, 216–218 (1998).
[53] Gu, M. and D. Morrish, "Three-dimensional trapping of Mie metallic particles by the use of obstructed laser beams," *J. Appl. Phys.* **91**, 1606–1612 (2002).

[54] Saija, R., P. Denti, F. Borghese, O. M. Maragò, and M. A. Iatì, "Optical trapping calculations for metal nanoparticles. Comparison with experimental data for Au and Ag spheres," *Opt. Express* **17**, 10231–10241 (2009).
[55] Hajizadeh, F. and S. N. S. Reihani, "Optimized optical trapping of gold nanoparticles," *Opt. Express* **18**, 551–559 (2010).
[56] Atlan, M., M. Gross, P. Desbiolles, É. Absil, G. Tessier, and M. Coppey-Moisan, "Heterodyne holographic microscopy of gold particles," *Opt. Lett.* **33**, 500–502 (2008).
[57] Absil, E., G. Tessier, M. Gross, M. Atlan, N. Warnasooriya, S. Suck, *et al*., "Photothermal heterodyne holography of gold nanoparticles," *Opt. Express* **18**, 780–786 (2010).
[58] Verpillat, F., F. Joud, P. Desbiolles, and M. Gross, "Dark-field digital holographic microscopy for 3D-tracking of gold nanoparticles," *Opt. Express* **19**, 26044–26055 (2011).
[59] Pham, Q. D., Y. Kusumi, S. Hasegawa, and Y. Hayasaki, "Digital holographic microscope with low-frequency attenuation filter for position measurement of nanoparticle," *Opt. Lett.* **37**, 4119–4121 (2012).
[60] Kerker, M., *The Scattering of Light and Other Electromagnetic Radiation*. (Academic Press, New York, 1969), Ch. 3.
[61] Bohren C. F. and D. R. Huffman, *Absorption and Scattering of Light by Small Particles*. (John Wiley & Sons, Inc., New York, 1983), Ch. 4.
[62] Goodman, J. W. *Introduction to Fourier Optics*, 2nd edn (McGraw-Hill, New York, 1996), Ch. 3.10.